THE JOURNAL OF PHYSICAL CHEMISTRY C

C: Energy Conversion and Storage; Energy and Charge Transport

Influence of Doping and Controlled Sn Charge State on the Properties and Performance of SnO Nanoparticles as Anodes in Li-Ion Batteries

Antonio Vázquez-López, David Maestre, Julio Ramírez-Castellanos, José M. González-Calbet, Igor Pis, Silvia Nappini, Neslihan Yuca, and Ana Cremades

J. Phys. Chem. C, **Just Accepted Manuscript** • DOI: 10.1021/acs.jpcc.0c06318 • Publication Date (Web): 27 Jul 2020

is published by the American Chemical Society. 1155 Sixteenth Street N.W., Washington, DC 20036

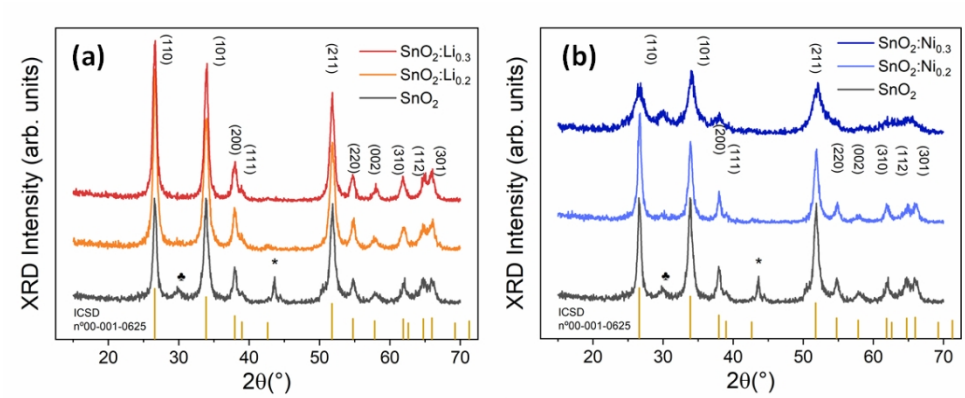

Fig 1: XRD patterns from (a) Li and (b) Ni doped SnO_2 nanoparticles. XRD pattern from undoped SnO_2 is also included as a reference. The peaks around 43.5-44° and 50° marked with (*) is due to the sample holder. The peak around 30° marked with (♠) is due to romarchite SnO.

321x130mm (96 x 96 DPI)

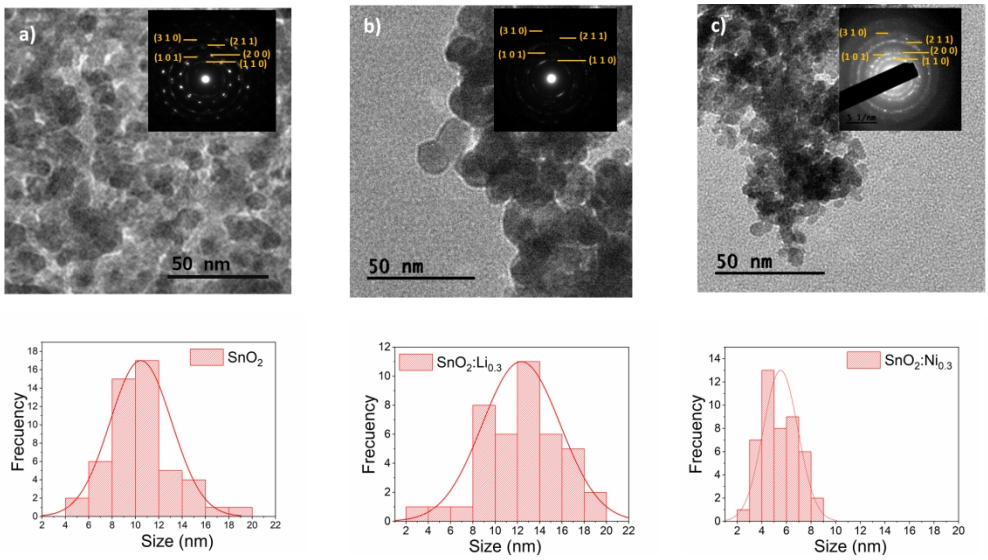

Fig 2: TEM image and SAED diffraction patterns from a) SnO_2 b) SnO_2:$Li_{0.3}$ c) SnO_2:$Ni_{0.3}$ nanoparticles. Underneath histograms with particle size for each sample are presented

602x331mm (96 x 96 DPI)

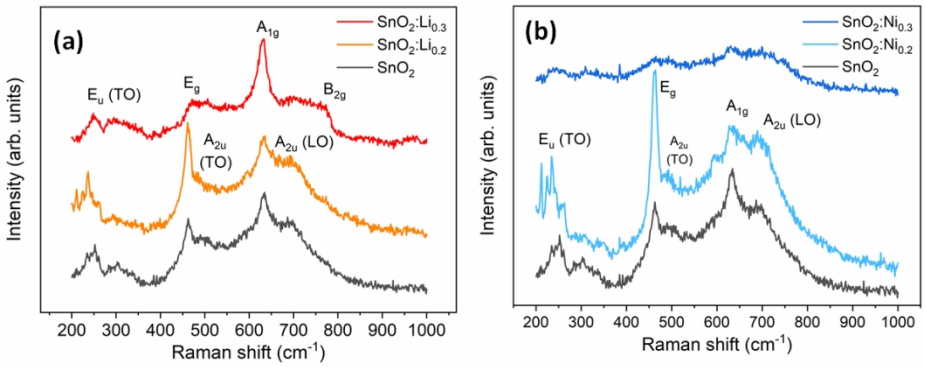

Fig 3: Raman spectra from (a) Li and (b) Ni doped SnO_2 nanoparticles. Raman spectrum from undoped SnO_2 is also included as a reference.

350x143mm (96 x 96 DPI)

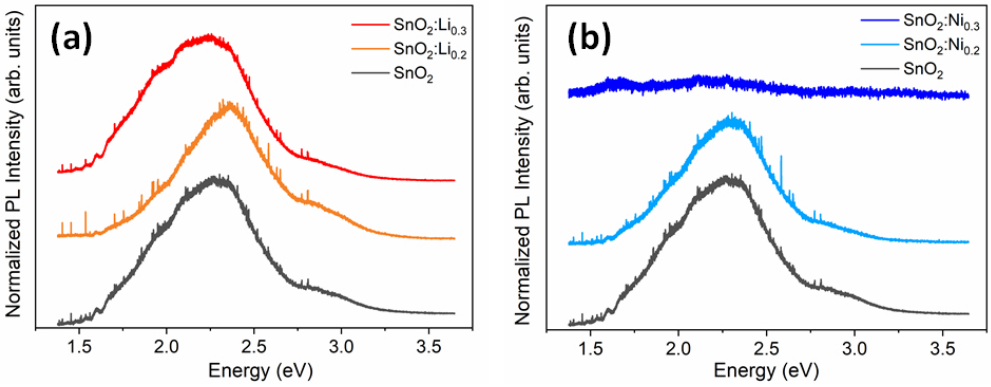

Fig 4: Normalized photoluminescence spectra from (a) Li and (b) Ni doped nanoparticles. PL spectrum from undoped SnO_2 nanoparticles is included as a reference.

250x97mm (96 x 96 DPI)

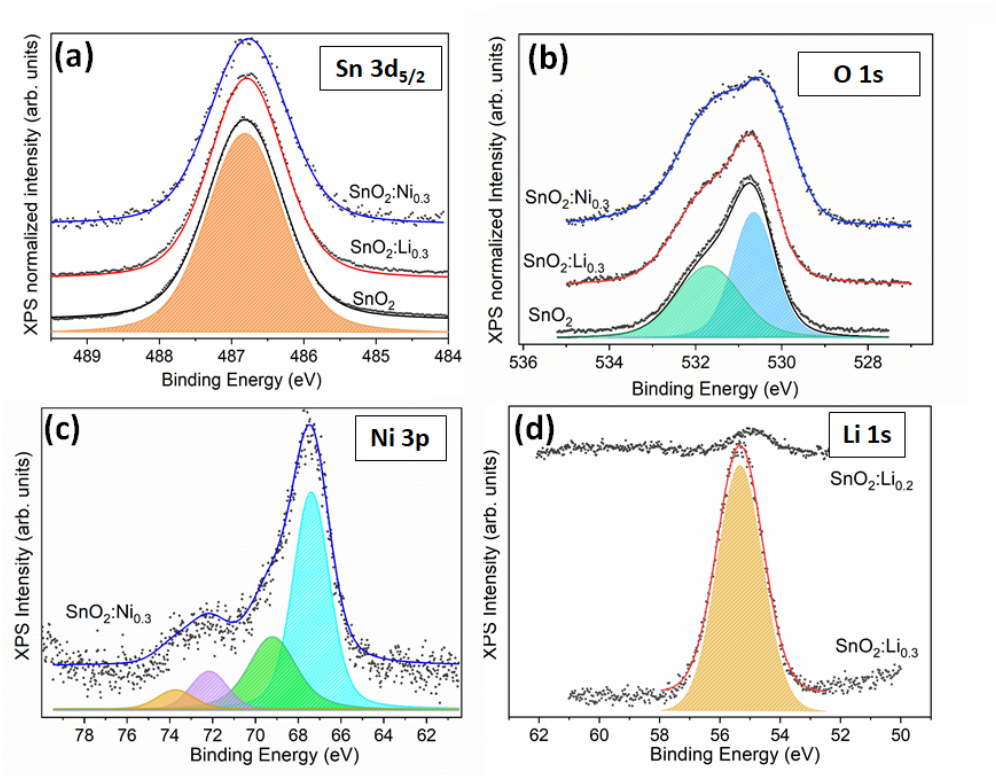

Fig 5: a) Sn($3d_{5/2}$), b) O(1s), c) Ni(3p) and d) Li(1s) XPS core levels from undoped and doped (Ni, Li) SnO_2 nanoparticles acquired with photon energy of 650 eV for Sn($3d_{5/2}$), O(1s) and Ni(3p), and photon energy of 253 eV for Li(1s).

230x181mm (96 x 96 DPI)

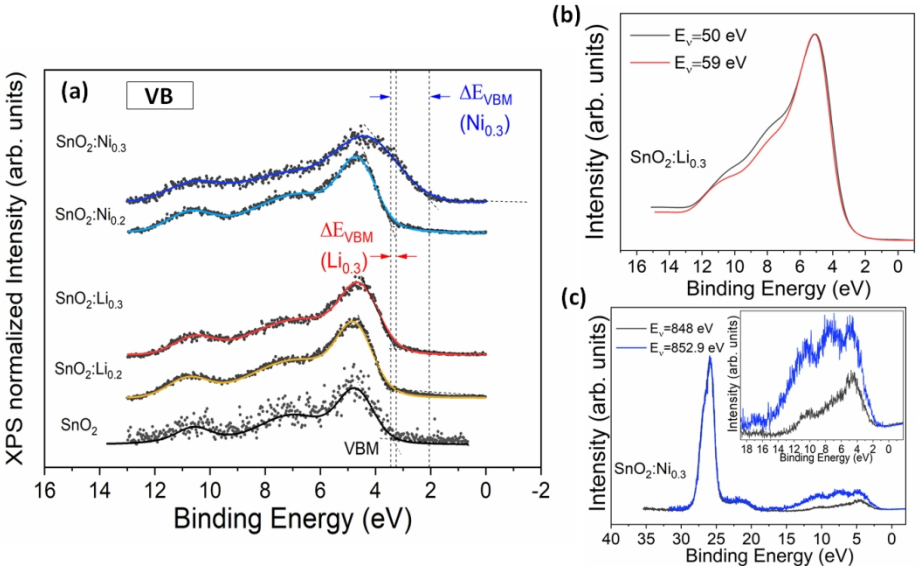

Fig. 6. a) Valence band spectra of undoped and Li, Ni doped SnO_2 nanoparticles acquired with a photon energy of 650 eV. b) valence band spectra of the sample SnO_2:$Li_{0.3}$ acquired under conditions of "off resonance" (E_v=50 eV) and "on-resonance" (E_v=59 eV). c) Valence band spectra of the sample SnO_2:$Ni_{0.3}$ acquired under conditions of "out of resonance" (E_v=848 eV) and "on-resonance" (E_v=852.9 eV) according to the Ni $L_{3,2}$ edge XAS spectrum in Figure S2.

388x223mm (96 x 96 DPI)

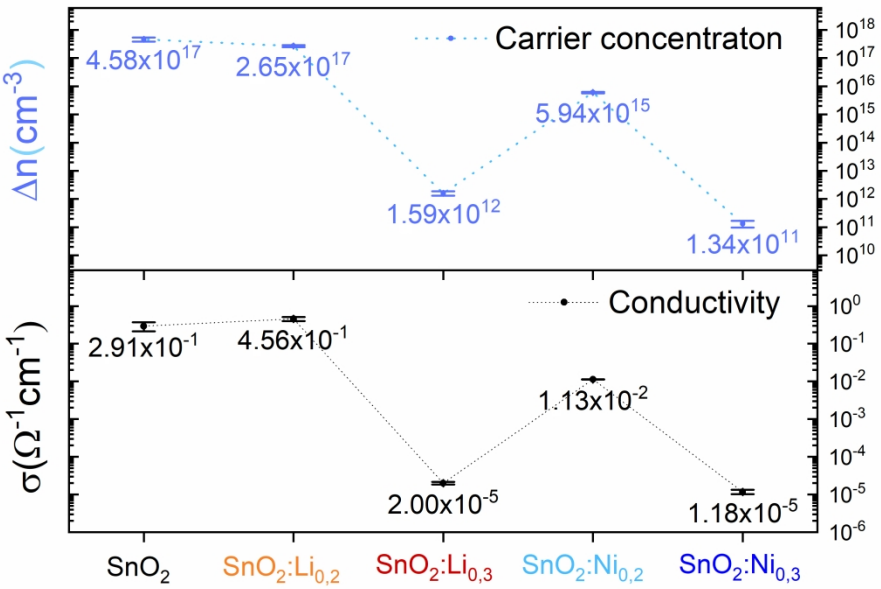

Figure 7. Variation in the charge carrier concentration and the conductivity of the undoped and doped SnO_2 nanoparticles as a function of the doping.

289x202mm (300 x 300 DPI)

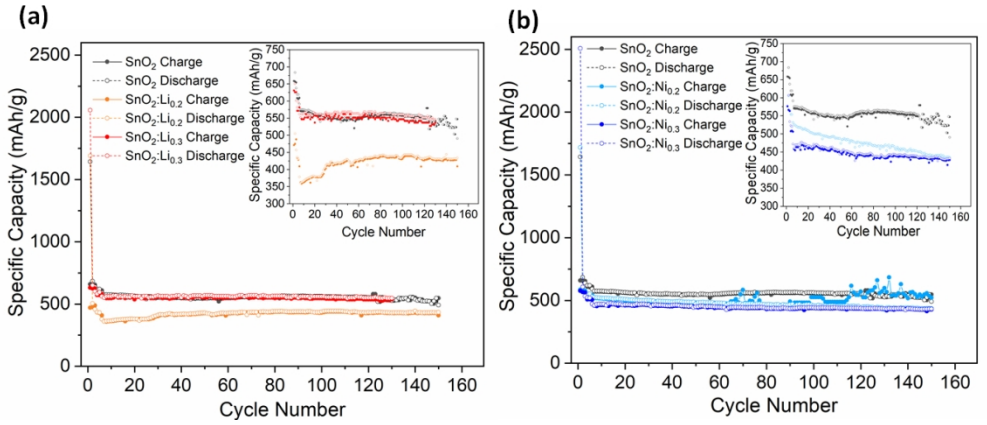

Fig. 8: Specific capacity values upon cycling from LiB with anodes based in (a) Li doped or (b) Ni doped SnO_2 nanoparticles. Values from undoped SnO_2 nanoparticles-based anodes are also included as a reference.

358x153mm (96 x 96 DPI)

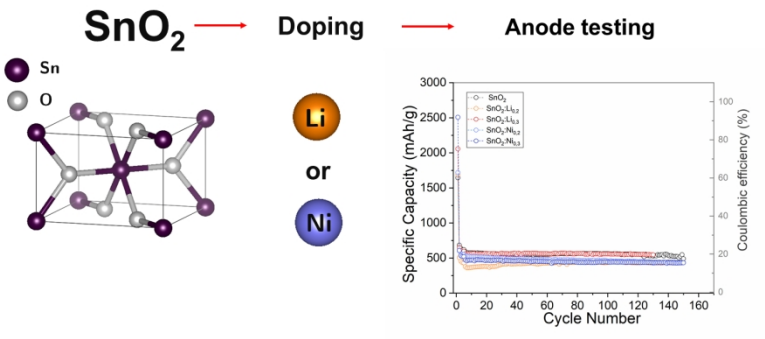

500x300mm (96 x 96 DPI)

Influence of doping and controlled Sn charge state on the properties and performance of SnO_2 nanoparticles as anodes in Li-ion batteries

Antonio Vázquez-López[a*], David Maestre[a], Julio Ramírez-Castellanos[b], José M. González-Calbet[b], Igor Píš[c,d], Silvia Nappini[d], Neslihan Yuca[e,f], and Ana Cremades[a]

[a] Departamento de Física de Materiales, Facultad de CC. Físicas, Universidad Complutense de Madrid, 28040, Madrid, Spain

[b] Departamento de Química Inorgánica, Facultad de CC. Químicas, Universidad Complutense de Madrid, Madrid, 28040, Spain

[c] Elettra-Sincrotrone Trieste S.C.p.A., S.S, 14 km 163.5, 34149 Basovizza, Trieste, Italy

[d] IOM-CNR, Laboratorio TASC, S.S. 14 km 163.5, 34149 Basovizza, Trieste, Italy

[e] Maltepe University, Marmara Eğitim Köyü 34857 Maltepe, Istanbul, Turkey

[f] Enwair Energy Technologies Corp., Sariyer, 34469, Istanbul Turkey

[*] corresponding author. E-mail:antvaz01@ucm.es

Abstract

Li-ion batteries (LiB) play nowadays a major role in several technological fields. In addition to enhanced high capacity and long cyclability, some other issues regarding safety, materials sustainability, and low-cost remain unsolved. Tin oxide (SnO_2) presents several of those advantages as an anode material, however some aspects still require to be investigated as the capacity fading over cycles. Herein, tin oxide nanoparticles-based anodes have been tested showing high capacities and a significant cyclability over more than 150 cycles. A complementary strategy introducing doping elements such as Li and Ni during the synthesis by hydrolysis has been also evaluated versus the use of undoped material, in order to assess the dependence of SnO_2 quality and properties on battery performance. Diverse aspects such Sn charge state in the synthesized nanoparticles, the variable incorporation of dopants, and the structure of defects have been considered in the understanding of the obtained capacity.

1. Introduction

One of the main challenges facing the energy storage field in recent years is focused on the improvement of the capacity and performance/cyclability of Lithium ion batteries (LiB), for which different materials and strategies are considered such as reducing sizes to the nanoscale [1,2], controlling the morphology and aspect ratio [3], using nanocomposites material [4,5], complex structures [3,6,7], and doping with different elements [8,9] among others. Diverse materials are being considered as alternative candidates to the graphite-based anodes so far. In this frame, tin oxide has been the focus of on-going research [10] due to the ability of intercalation lithium and its great electrochemical behaviour, being abundant, low-cost, environmental friendly and safe during performance. Hence, significant efforts have been made in the optimization of the synthesis methods leading to SnO_2 with controlled dimensions, morphology and concentration of lithium or other dopants, which are key factors to achieve efficient working devices. However, despite the different anode compositions, complex structures, and multiple testing conditions reported in the literature, some limitations still require to be overcome, as its volume expansion and the usual capacity fading upon long cycling. Regardless of the great efforts that are being focused on the comprehension of the reaction mechanisms occurring during the battery operation, the quality of the initial SnO_2 nanomaterial is not usually considered as a pivotal parameter of the performance equation. Nonetheless, point defects such as oxygen vacancies, unintentional impurities, dopants, and cationic charge states could play an important role either inhibiting or enhancing the intermediate reactions and the final electrochemical performance.

Different synthesis methods have been reported so far for the synthesis of SnO_2 nanoparticles, such as hydrothermal [11], sol-gel [12], chemical vapour deposition (CVD)[13], co-precipitation [14], or synthesis methods based on polymeric precursors, among others, which usually lead to SnO_2 nanomaterial with a certain ratio of Sn^{2+} to Sn^{4+} concentration [15] and variable structure of defects. As an example, some of our recent works demonstrated the different distribution of defects in lithium-doped SnO_2 nano and bulk materials [16–19], the

surface properties of which are also affected by the selected synthesis method. Therefore, it is mandatory to find an easy, reliable, and scalable method able to synthesize large amounts of SnO_2 nanomaterial with high crystallinity, allowing size and composition control, as well as enabling tunability of defects and surface properties, in order to face the challenge of transitioning the fundamental advances in LiB to the commercial use.

In this work we synthesized undoped SnO_2 and Lithium or Nickel doped SnO_2 nanoparticles via a hydrolysis method which allows the synthesis of large amount of nanomaterial with controlled dimensions and variable properties as a function of the selected dopant. Doping with Li and transition metals (such as Ni) can lead to variations in the SnO_2 electrical conductivity and the optical absorption. In addition, incorporation of dopants can also alter the synthesis process favouring or hindering the growth of nanoparticles and the formation of defects, which should be also considered in this case [15,20]. Actually, Li doped SnO_2 has demonstrated promising performance in Li-ion batteries based on the enhanced lithiation and insertation-desinsertation of Lithium. Moreover, the use of some other metal dopants can also improve the battery response. Some authors [21,22] exposed that the use of Iron or Cobalt doped SnO_2 involves good specific capacity and enhanced coulombic efficiency. In the present work, the use of both Li doped SnO_2 and Ni doped SnO_2 has been evaluated in order to assess the role played by these dopants in the modification of the SnO_2 properties and the performance of LiB devices.

A throughout characterization of the undoped and doped (Ni, Li) SnO_2 nanoparticles has been carried out in this work by means of x-ray diffraction (XRD), transmission electron microscopy (TEM), selected area electron diffraction (SAED), energy dispersive x-ray spectroscopy (EDS), inductively coupled plasma-optical emission spectrometry (ICP-OES), photoluminescence (PL), Raman spectroscopy, Hall-effect measurements, and finally x-ray photoelectron spectroscopy (XPS) and x-ray absorption spectroscopy (XAS). The performance of these nanoparticles as anodes in Li ion battery was also evaluated and discussed.

2. Experimental section

2.1. SnO_2 nanoparticles synthesis

In this work, the synthesis of SnO_2 nanoparticles has been carried out by hydrolysis, which allows to obtain a large quantity of material with good control in size and final composition of the nanoparticles. Firstly, undoped SnO_2 nanoparticles were synthesized using $SnCl_2 \cdot 2H_2O$ (Sigma Aldrich purity 99.99%) as precursor. After dissolution of the precursor in water and continuous stirring at 50 °C, NH_4OH was added until pH = 8 was reached and distilled water was added to induce the hydrolysis process. Then, the temperature was increased up to 100 °C for 2 h. The obtained product was centrifuged until reaching neutral pH and subsequently dried at 50 °C for 12 h. Finally, the hydrolysis product, which corresponds to romarchite SnO, was calcinated at 350 °C for 20 h in order to obtain cassiterite (rutile) SnO_2 nanoparticles.

For the synthesis of the SnO_2 nanoparticles doped with Ni or Li, stoichiometric amounts of $NiCl_2 \cdot 6H_2O$ (Probus) or LiCl (Labkem purity 99%), respectively, were also added to $SnCl_2 \cdot 2H_2O$ and diluted in distilled water. The rest of the synthesis is analogous to that followed for the synthesis of the undoped nanoparticles.

The corresponding nomenclature used for the synthesized nanoparticles is SnO_2:Y_x, where Y denotes the dopant (Li or Ni), and x= 0.2 and x = 0.3, denotes the selected initial concentrations of the dopants in the precursor mixture, corresponding to 20 % and 30 % in weight. Hereinafter, the samples will be referred to as SnO_2:$Li_{0.2}$, SnO_2:$Li_{0.3}$, SnO_2:$Ni_{0.2}$, and SnO_2:$Ni_{0.3}$ respectively, while the undoped sample will be named as SnO_2.

2.2. Cell preparation

In order to study its possible use as batteries, battery cells were prepared and assembled. For the cell preparation, Celgard 2400 separator was obtained from Celgard PAA (Mw: 450.000, Sigma Aldrich) was utilized as binder. Lithium-ion electrolyte was purchased from BASF, including 1.2 M lithium hexafluorophosphate ($LiPF_6$) in ethylene carbonate (EC), diethyl carbonate (DEC) (EC/DEC = 3:7 by weight), and 30 % by weight of fluoroethylene carbonate (FEC). After testing different compositions for the electrode, the results presented here correspond to SnO_2 based active materials, binder, and carbon black (CB) mixed in water with the optimized weight ratio of SnO_2 nanoparticle/PAA/CB =

70/20/10 for 3 hours. Slurries were coated on the copper foil by using a doctor blade. After electrodes dried, they were cut as disk for coin cell assembling. They were placed under a controlled atmosphere in the glovebox overnight and further dried in the vacuum oven at 90°C for 12 h to completely remove the water.

2.3. Characterization techniques

The structural characterization of the nanoparticles was carried out by X-ray diffraction (XRD) in a PANanalytical X'Pert Powder equipment, using the Cu Kα line where λ_{Cu} = 1.5404 Å. The microstructural analysis was performed in a transmission electron microscope (SAED / TEM) JEM 1400 plus JEOL. The compositional analysis was obtained by energy dispersive x-ray spectroscopy (EDS) with an EDX Bruker AXS 4010 analyzer coupled to the scanning electron microscope (SEM) Leica 440 Stereoscan. Detection and semiquantification of lithium was performed by Optical Emission Spectrometry (ICP-OES) in an ARCOS equipment from SPECTRO with excitation source ICP, Perkin Elmer Optima 3300DV. Three specimens for each sample were analysed in order to minimize the statistical error in the Li quantification. Photoluminescence (PL) and Raman spectroscopy measurements have been studied at room temperature in a confocal microscope Horiba Jobin Yvon LabRam Hr400 system using a He-Cd UV laser (λ = 325 nm) as excitation source and collected by charge coupled device (CCD). X-ray photoelectron (XPS) and absorption (XAS) spectroscopy have been performed at the CNR Beamline for Advanced diCHroism (BACH) [23,24] of the Elettra synchrotron facility in Trieste, Italy. Photoemission spectra were acquired with a Scienta R3000 electron energy analyzer in normal emission geometry with a total energy resolution of 180 meV. The XAS measurements were performed in total electron yield (TEY) by measuring the drain current through the sample. The photon energy resolution was set to 0.15 eV at Ni $L_{3,2}$-edge and O K-edge; 0.1 eV at Sn $M_{5,4}$ edge. For the electrical characterization, Hall effect measurements were performed on a Hall Ecopia AMP55T with 4 gold probes and using an HMS-7000 control electronics.

For cell preparation and test procedure, the electrodes were used to assemble the coin cells. As a counter electrode, Li metal was used. The performance of the assembled 2032 coin

cells was evaluated with Neware Battery Test system. The cut-off voltage of cell testing is between 1.2 V and 0.01 V, assuming a theoretical value of ~1500 mAh/g for SnO_2. Half cells were cycled at C/25 for 2 cycles, at C/10 for 2 cycles and at C/5 for 150 cycles.

3. Results and discussion

Both undoped and doped (Li, Ni) SnO_2 nanoparticles were initially characterized by XRD as shown in Figure 1. All the XRD patterns can be indexed according to the cassiterite structure of SnO_2, tetragonal unit cell, symmetry group $P4_2/mnm$, with lattice parameters close to a = b = 4.738 Å and c = 3.186 Å (ICSD: 00-001-0625). The XRD results confirm the high crystallinity of the as-synthesized nanoparticles, even for those with the highest amount of dopants. Peaks from the precursors or different secondary compounds were not observed for Li doped samples. In the undoped SnO_2 and the Ni doped samples, a weak peak around 30° corresponding to a small amount of romarchite SnO (ICSD: 01-072-1012) obtained during the synthesis can be observed, as marked in Figure 1. By using calcination temperatures higher than that employed in this work, 350 °C, the presence of SnO would be completely removed, although larger SnO_2 nanoparticles will be obtained instead. The broadening of the XRD peaks observed in Figure 1, mainly for the SnO_2:$Ni_{0.3}$ sample, indicates the low dimensions obtained for the synthesized nanoparticles.

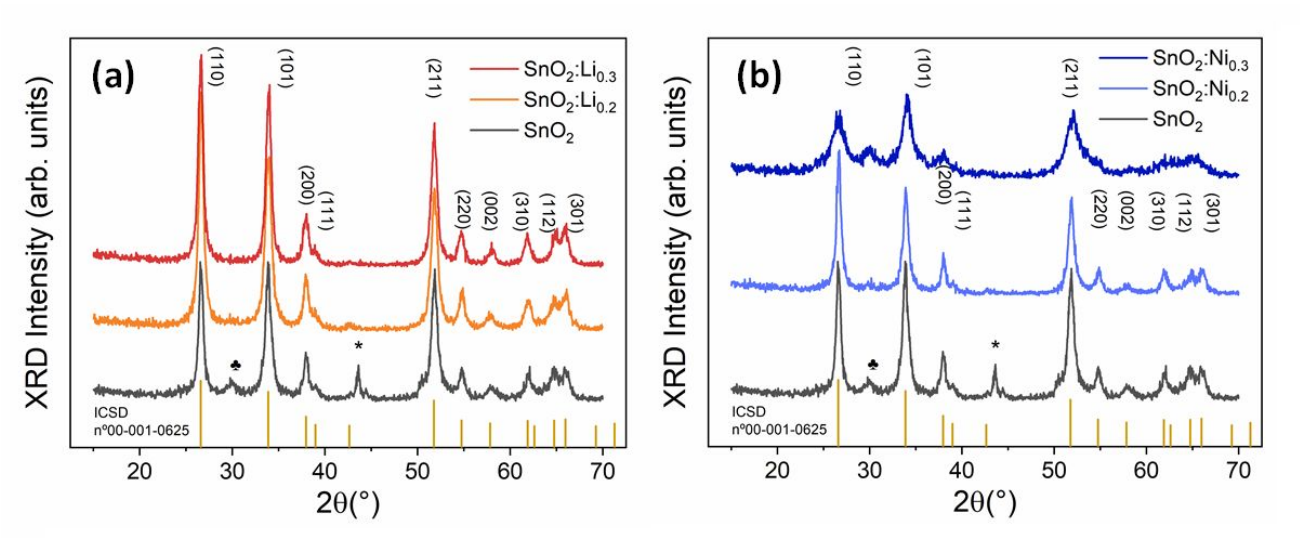

Fig 1: XRD patterns from (a) Li and (b) Ni doped SnO_2 nanoparticles. XRD pattern from undoped SnO_2 is also included as a reference. The peaks around 43.5-44° and 50° marked with (*) is due to the sample holder. The peak around 30 ° marked with (♣) is due to romarchite SnO.

The average crystallite dimensions (D) were estimated from the XRD patterns analysis by using the Scherrer formula $D = 0.89\lambda/Bcos(\theta)$, where B is the full width at half maximum (FWHM) of the diffraction maxima, λ is x-ray wavelength, $K = 0.89$ is the Scherrer factor, and θ corresponds to the Bragg angle. Table 1 shows the lattice parameters and the crystallite size estimated from the XRD analysis.

Table 1: Size estimation of the undoped and doped SnO_2 nanoparticles and the corresponding lattice parameters obtained from XRD analysis.

Sample	**Size (nm)**	**a(Å)**	**c(Å)**	**ratio c/a**	**V (Å^3)**
SnO_2	10.45 ± 0.05	4.73(8)	3.19(4)	0.674±0.001	71.70±0.26
SnO_2:$Li_{0.2}$	9.76 ± 0.03	4.74(2)	3.18(3)	0.671±0.001	71.58±0.09
SnO_2:$Li_{0.3}$	11.19 ± 0.03	4.73(0)	3.18(6)	0.673±0.001	71.28±0.12
SnO_2:$Ni_{0.2}$	10.62 ± 0.05	4.73(3)	3.18(7)	0.673±0.001	71.40±0.19
SnO_2:$Ni_{0.3}$	7.29 ± 0.05	4.72(3)	3.16(4)	0.670±0.001	70.59±0.13

Undoped SnO_2 nanoparticles show averaged crystallite dimensions around 10 nm. Slight changes were detected in the estimated crystallite sizes as a function of the doping. This effect is more noticeable for the case of the Ni doped nanoparticles for which the crystallite dimensions decreases down to 7.29 nm for the nanoparticles with the highest amount of Ni (SnO_2:$Ni_{0.3}$). Previous studies indicated that the inhibition or promotion of the growth kinetics of nanoparticles depends on the precursors used during hydrolysis. In this case, the presence of the precursors used for the synthesis of the Ni doped nanoparticles could retard the kinetics of the growth process, as also reported for other doped SnO_2 nanoparticles [25]. The size of the SnO_2 unit cell slightly decreases with the incorporation of both Li and Ni, although the decrease in the lattice parameters is higher for Ni doping. Considering the ionic radii of Li^+ and Sn^{4+} in octahedral coordination and high spin configuration (R_{Li+} = 0.59 Å, R_{Sn4+} = 0.71 Å) [26], this effect can be due to the incorporation of Li^+ as substitutional of Sn^{4+}. The ionic radius of Ni^{2+} is similar to that from Sn^{4+} (R_{Ni2+} = 0.69 Å) [27], hence in this case partial incorporation of Ni as Ni^{3+}, with a lower radius than Ni^{2+}, should be also considered.

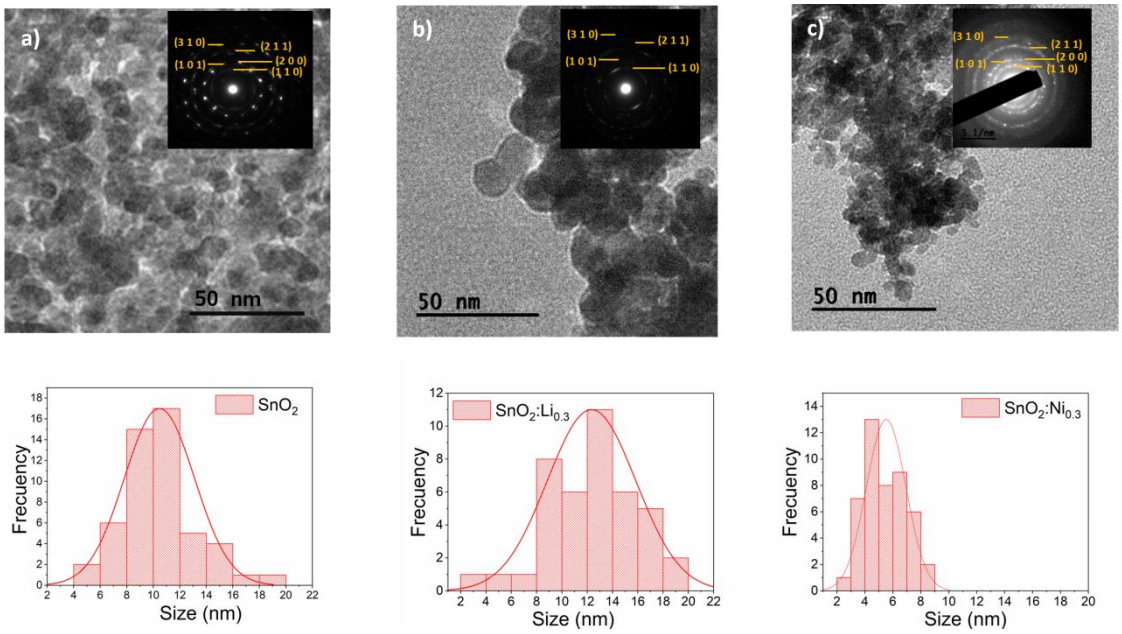

Fig 2: TEM image and SAED diffraction patterns from a) SnO_2 b) SnO_2:$Li_{0.3}$ c) SnO_2:$Ni_{0.3}$ nanoparticles. Underneath histograms with particle size for each sample are presented.

TEM micrographs (Figure 2) show that the SnO_2 nanoparticles exhibit rounded appearance and homogeneous dimensions around 10 nm. The dimensions of the doped nanoparticles decrease, mainly for the highest Ni doping (Figure 2c), in agreement with the XRD results. Histograms have been performed from TEM images in order to estimate the averaged particle dimensions which correspond to 10.5±2.8 nm for SnO_2, 12.3±3.4 nm for SnO_2:$Li_{0.3}$ and 5.4±1.6 nm for SnO_2:$Ni_{0.3}$. These values further agree with XRD results.

The corresponding SAED patterns (insets in Figure 2) confirm the crystallinity of the undoped and doped SnO_2 nanoparticles.

Table 2: Compositional analysis of the samples via EDS and ICP-OES of the doped samples.

EDS		**ICP-OES**	
Sample	% at.	Sample	% at.
SnO_2:$Ni_{0.3}$	3.9±0.3	SnO_2:$Li_{0.3}$	0.95±0.02
SnO_2:$Ni_{0.2}$	0.5±0.1	SnO_2:$Li_{0.2}$	0.06±0.03

To estimate the amount of Ni incorporated in the SnO_2 nanoparticles, the EDS technique was employed. As Li is a light element, the quantification of which is not straightforward. ICP-OES measurements were carried out for the analysis of Li doping. The estimated atomic percentages of Ni and Li are included in Table 2. The final amount of dopants varies from 0.5 to 3.9 % at. for the Ni doped samples, and from 0.06 to 0.95 % at. for the Li doped ones.

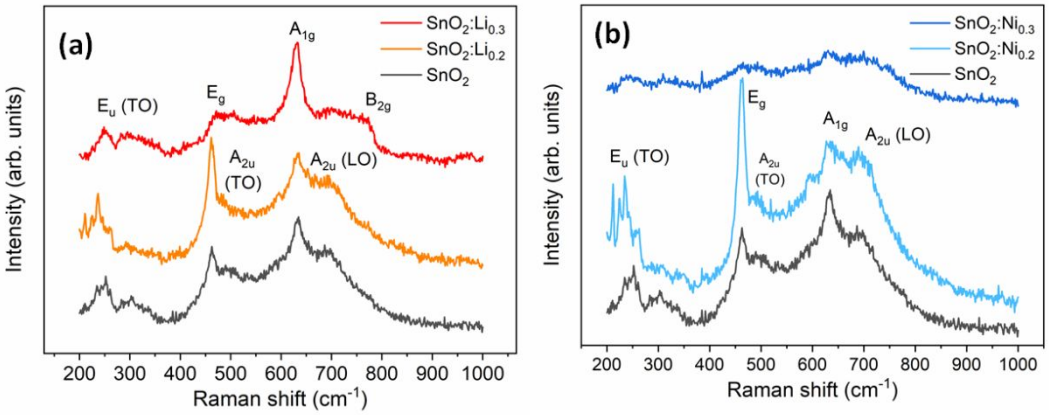

Fig 3: Raman spectra from (a) Li and (b) Ni doped SnO_2 nanoparticles. Raman spectrum from undoped SnO_2 is also included as a reference.

Raman spectra for the undoped and doped nanoparticles are shown in Figure 3. All the peaks in the Raman spectra can be assigned only to vibrational modes from rutile SnO_2. Tin oxide presents two active IR modes (A_{2u}, E_u), four Raman active modes (A_{1g}, B_{1g}, B_{2g}, E_g), and two inactive modes (A_{2g}, B_{1u}). It is commonly reported that E_g (490 cm^{-1}), A_{1g} (640 cm^{-1}) and B_{2g} (760 cm^{-1}) modes usually dominate the SnO_2 Raman spectra. These modes are associated with the movement of O anions along the c axis (E_g), and elongation of O-Sn-O and movement of the anions in a symmetric (A_{1g}) and asymmetric manner (B_{2g}) orthogonal to the c axis. However, by reducing the dimensions of SnO_2 and/or increasing the lattice disorder, modification of the Raman modes, as well as activation of inactive modes, can be promoted. In this work, the Raman spectrum from undoped SnO_2 nanoparticles presents main contributions at around 240 cm^{-1}, 460 cm^{-1} and 640 cm^{-1} which can be associated with E_u (TO), E_g and A_{1g} modes, respectively. Besides, weak peaks at around 300 cm^{-1}, 500 cm^{-1} and 690 cm^{-1} can be also observed in Figure 3. The low frequency modes can be assigned to IR active E_u(TO) mode in SnO_2, as reported in [28], while for the mode at 500 cm^{-1} an origin related to IR active A_{2u} TO mode is considered. Activation of inactive Raman modes owing to relaxation of the Raman selection rules in SnO_2 has been commonly reported for nanoparticles. Diéguez et al. [29] reported modes in this region associated with disorder in SnO_2 nanoparticles, probably due to a high concentration of oxygen vacancies. The high wavenumber mode at around 690 cm^{-1} is related to the IR active A_{2u} (LO) mode. In this case, the B_{2g} (780 cm^{-1}) mode is not observed for the undoped SnO_2 nanoparticles, probably due to the presence of defects that hinder this vibrational mode. Variations in these Raman modes can also be observed as a function of the doping, even for the lowest dopant concentration.

Low Li doping induces an increase in the relative intensity of the E_g mode which dominates the corresponding spectrum. By increasing the amount of Li, a decrease in the relative intensity of the E_g and A_{2u} modes can be observed, while the A_{1g} mode increases. These modes involve vibration of oxygen either along the c-axis (E_g) or stretching of O anions respect to Sn orthogonally to the c-axis (A_{1g}). In addition, contrary to the rest of samples,

the B_{2g} mode at around 780 cm^{-1} can be distinguished for the sample with the highest amount of Li. This mode is related to the comprising motions of O anions with respect to Sn cations perpendicular to the c-axis. Thereby, incorporation of Li in the SnO_2 lattice in a low concentration promotes vibrational modes related to motion of O along the c-axis, while higher amount of Li induces an increase of the vibrational modes perpendicular to the c-axis (A_{1g}, B_{2g}). Moreover, the appearance of the B_{2g} mode only in the samples with the highest amount of Li can be associated with a decrease in the concentration of lattice defects, which mitigates this vibrational mode for the rest of samples.

On the other hand, low Ni doping induces an increase in the relative intensity of the E_g mode at ~ 460 cm^{-1} and a decrease in the relative intensity of the A_{1g} mode, which allows to distinguish a weak contribution at around 600 cm^{-1}. In the low-wavenumber region, a more complex contribution around 240 cm^{-1} can be observed together with weak modes at 300 and 340 cm^{-1}. These modes could be related to TO and LO IR- E_u modes, which is triple-degenerated. By increasing Ni doping, the corresponding Raman spectrum exhibits less defined contributions, with a drastic decrease in the relative intensity of the E_g mode, which in this case seems to be highly sensitive to the Ni doping. A higher concentration of defects in the smallest SnO_2:$Ni_{0.3}$ nanoparticles can be related to the decrease of the corresponding Raman signal. Sn^{4+} substitution by Ni^{2+}, with similar ionic radii, is commonly reported for Ni doping, although the presence of Ni^{3+} should be also considered in this case, in agreement with XRD measurements, thus inducing variable structure of defects in SnO_2 in order to achieve charge balance.

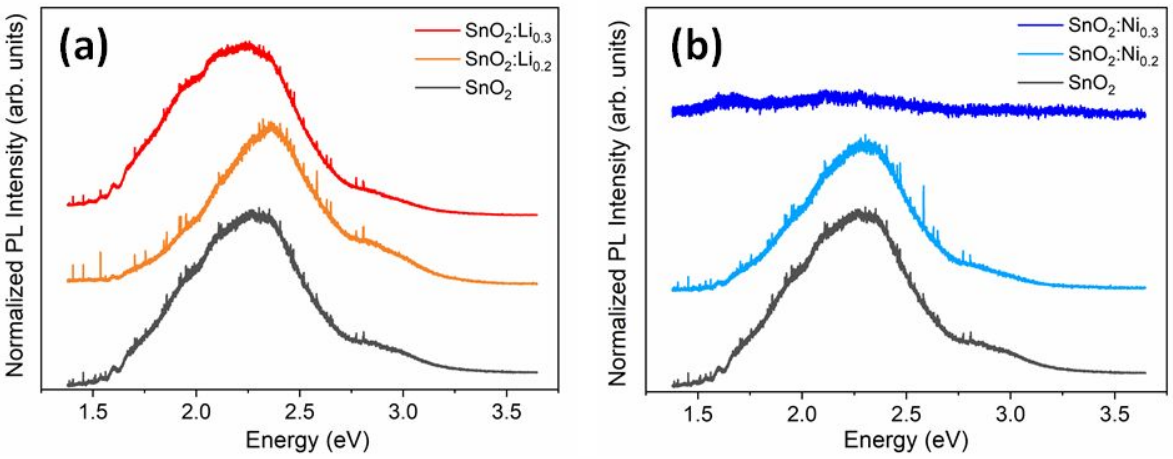

Fig 4: Normalized photoluminescence spectra from (a) Li and (b) Ni doped nanoparticles. PL spectrum from undoped SnO_2 nanoparticles is included as a reference.

The luminescent properties of the SnO_2 nanoparticles employed in the LiB anodes were analyzed by photoluminescence using and UV laser (λ= 325 nm) as excitation source, as shown in Figure 4. The characteristic luminescence of SnO_2 is usually centered in the visible range and three main emissions are distinguished: the so-called orange band (1.94 eV) associated with defect states due to oxygen vacancies, the green band (2.25 eV) normally associated with oxygen vacancies with two adjacent oxygen atoms missing [30], and the blue one (2.58 eV) related to transitions involving surface states. In this work, undoped SnO_2 nanoparticles show a broad PL spectrum from the near-IR to the UV range centered around 2.3 eV. Deconvolution of this PL signal (shown in Supplementary Figure S1) indicates the presence of bands at 1.6 eV, 1.9 eV, 2.3 eV, 2.6 eV and 2.9 eV. The high relative intensity of the orange and green bands (1.9, 2.3 eV) associated with oxygen vacancies indicates the presence of these native defects in the probed SnO_2 nanoparticles. The low energy band at 1.6 eV has been also reported for doped SnO_2 and could be attributed to intrinsic defects promoted by doping which mechanism could be explained by the presence of Sn-interstitial defect level [31]. The high energy emission at 2.9 eV can be related to recombination of an electron from the conduction band with a $V_o^{\cdot\cdot}$ center [32].

Variable Li doping leads to changes in the SnO_2 luminescence signal. Either a decrease or an increase of the relative intensity from the orange and green bands, related to oxygen vacancies, was induced by low or high Li doping, respectively. Hence, different incorporation of Li into the SnO_2 lattice, as well as related defects, should be promoted as a function of the amount of Li, in agreement with the analysis of the Raman signal. Actually, incorporation of Li in substitutional Sn^{4+} sites can induce formation of oxygen vacancies to maintain charge neutrality, which related emission is enhanced for SnO_2:$Li_{0.3}$.

Doping with a low amount of Ni only induces slight changes in the corresponding PL signal, dominated by the green emission (2.25 eV), with respect to undoped SnO_2. However, by increasing the amount of Ni a drastic quenching of the luminescence is observed. This effect is known as "killer effect", characteristic of the transition metals of the Fe group, highlighting a strong effect for the Ni^{2+} ions [33]. Hence, the decrease of the emission intensity for SnO_2:$Ni_{0.3}$ may be a result of the formation of a large number of non-radiative recombination centres by Ni incorporation [34].

XPS and XAS measurements were also performed in the undoped and Li, Ni doped nanoparticles.

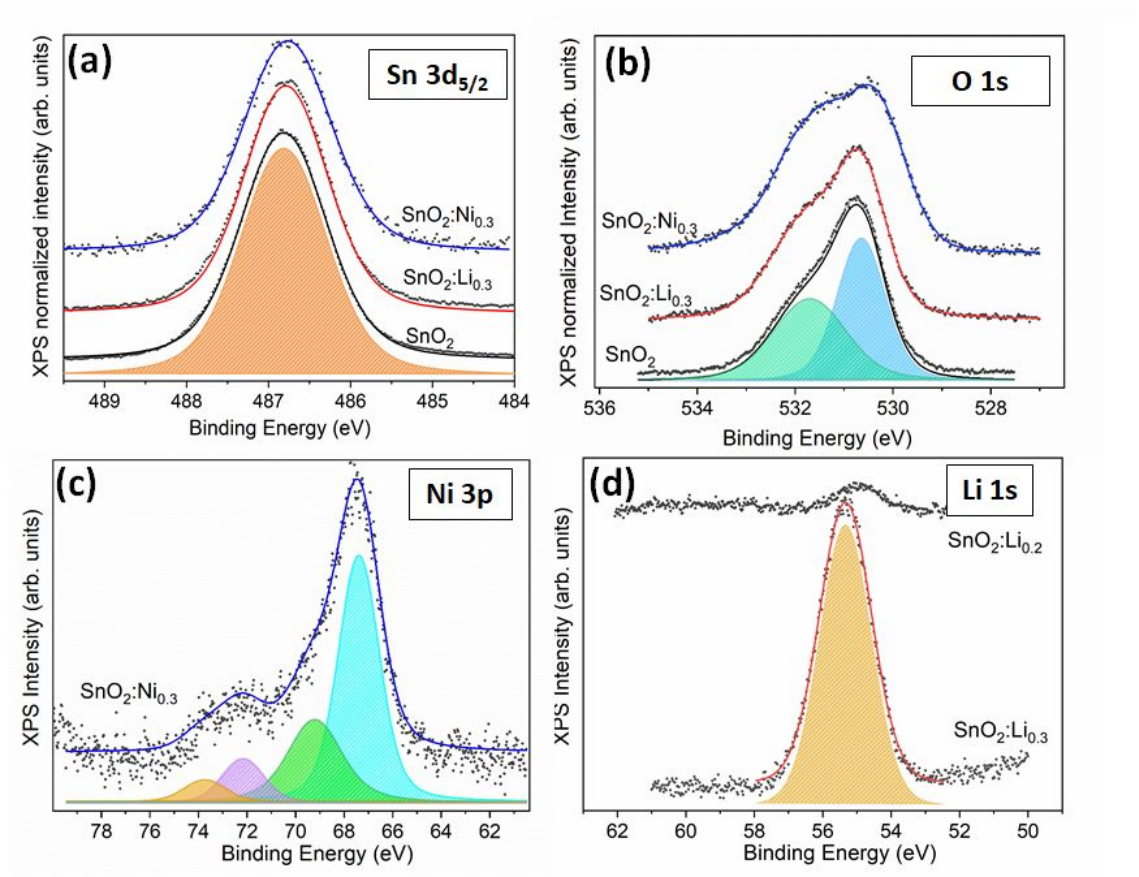

Fig 5: a) Sn($3d_{5/2}$), b) O(1s), c) Ni(3p) and d) Li(1s) XPS core levels from undoped and doped (Ni, Li) SnO_2 nanoparticles acquired with photon energy of 650 eV for Sn($3d_{5/2}$), O(1s) and Ni(3p), and photon energy of 253 eV for Li(1s).

The XPS spectra in Figure 5 were calibrated using the C(1s) core level from adventitious carbon at 284.6 eV. After Shirley background correction, Voigt functions were used for the deconvolution of the spectra. Both for undoped and doped (Ni, Li) samples, Sn $3d_{5/2}$ and $3d_{3/2}$ contributions appear at binding energies about 486.8 eV and 495.2 eV, respectively, with an energy difference around 8.41 eV, corresponding to the main charge state of Sn^{4+} in rutile type SnO_2 [35,36]. Figure 5a shows the Sn $3d_{5/2}$ core levels from the analyzed samples, in which one only contribution at 486.8 eV due to Sn^{4+} in rutile SnO_2 [37] can be observed both for undoped and doped (Ni, Li) SnO_2 nanoparticles. Despite the small amount of SnO detected by XRD, in this case contributions from Sn with lower oxidation states were not detected in the XPS spectra, which can be due to the different depth resolution of the techniques. XPS is more surface sensitive than XRD, hence among other possibilities, a

possible SnO/SnO_2 core shell structure formed in some nanoparticles due to the easy oxidation of SnO, or the low presence of SnO-like domains in intergranular regions could be considered. In any case, the presence of SnO should be very weak and most of the nanoparticles correspond only to SnO_2, as confirmed by XPS. Some works [38] commonly reported an unavoidable presence of a Sn^{2+} band at lower binding energies in the XPS spectra from SnO_2, which is usually related to regions with electronic environment similar to SnO due to a high oxygen deficiency. In this work, neither the presence of Ni nor Li doping induces reduced states of Sn, at least within the detection limit of the technique, and only Sn^{4+} is observed in the XPS study, which confirms the high crystalline quality of the as-synthesized SnO_2 nanoparticles.

Figure 5b shows the O(1s) core levels for undoped and doped samples. The spectra can be deconvoluted in two main contributions O_I centered at 530.6 eV, due to oxygen in SnO_2, and O_{II} at 531.7 eV, associated with oxygen defect states and with the presence of adsorbed oxygen at the surface and oxyen deficiency [35]. In some works the high energy peak is also associated with the presence of –OH groups [28]. The relative intensity of the contribution at 531.7 eV due to lattice oxygen increases with the addition of both Ni and Li dopants. Thereby, higher dopant concentration induces an increase in the O_{II}/O_I ratio, as observed in Figure 5b mainly for the Ni doped SnO_2, which can be related to the enhanced oxygen adsorption due to the lower dimensions and higher surface-to-volume ratio of these SnO_2:$Ni_{0.3}$ nanoparticles, as demonstrated by XRD and TEM, as well as a slight increase in the concentration of oxygen vacancies at the surface of these doped nanoparticles.

Figure 5c shows the Ni(3p) core level for SnO_2:$Ni_{0,3}$ in which the splitting of Ni(3p) into Ni $3p_{½}$ and Ni $3p_{3/2}$ can be observed. Peaks centered at 67.4 eV and 69.2 eV can be attributed to the presence of Ni^{2+}, while the contributions at higher energy correspond partially to Ni^{3+} [39]. The proposed peaks match the position, doublet separation and intensity of a doublet due to spin orbit interaction. This result confirms that Ni is incorporated with a variable oxidation state in SnO_2, although due to the complexity of the Ni(3p) signal, quantification is avoided in this case. Actually it should be noted that the fitting at higher energies with the proposed peaks is not matching completely the total XPS signal, as the region of higher energies could contain satellite peaks [40]. Atomic multiplet splitting and

charge transfer effects could contribute to satellite peaks about 5 to 6 eV from the Ni(3p) main peaks [41] which have not been added to the deconvolution for the sake of clarity. Still, some controversy remains about the multivalence of Nickel analysis in Ni 3p spectra, as some authors atribute peaks between 67 and 69 for both Ni^{2+} and Ni^{3+} [42], while in some other cases only Ni^{2+} is considered.

The Li(1s) core levels from the Li doped SnO_2 samples are shown in Figure 5d. The XPS spectra are centered at 54.9 eV for the sample SnO_2:$Li_{0.2}$ and 55.3 eV for SnO_2:$Li_{0.3}$ which correspond to Li^+, thereby confirming Li doping in the samples. As expected, based on the comparison of the Li 1s intensity ratio, Li concentration is lower for the SnO_2:$Li_{0.2}$, in agreement with the ICP-OES measurements. The shift observed in the binding energy from Li(1s) as a function of the amount of dopant could be due to the variable incorporation of Li as interstitial and/or substitutional [43,44], which is in agreement with the Raman and PL signals. Based on these results, insterstitial Li could be promoted by low Li doping, while higher Li doping would also induce subtitutional Li.

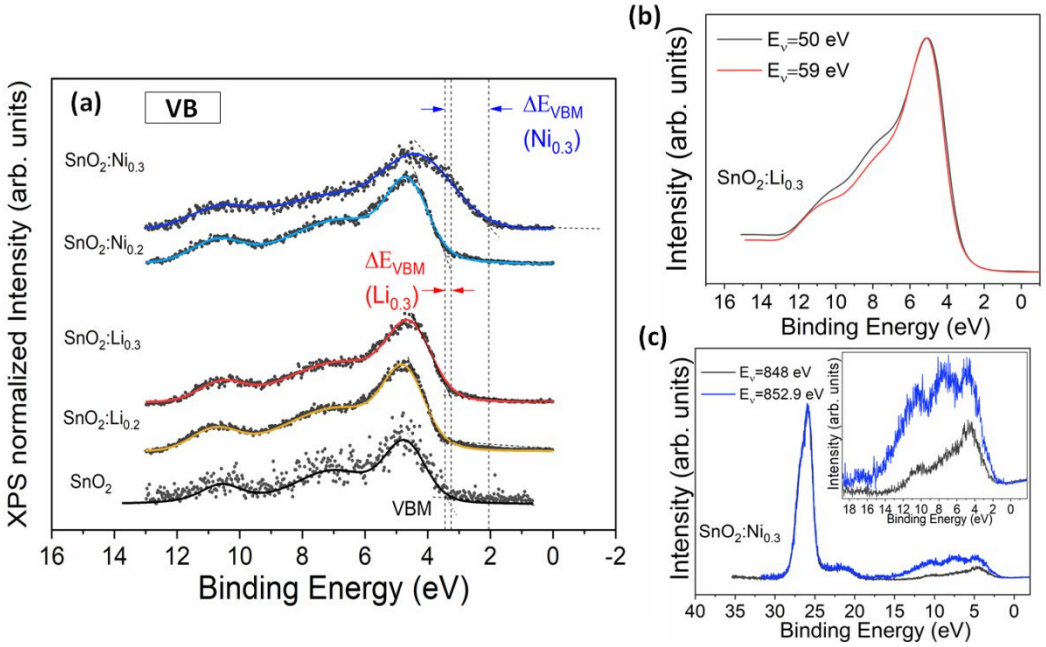

Fig. 6. a) Valence band spectra of undoped and Li, Ni doped SnO_2 nanoparticles acquired with a photon energy of 650 eV. b) Valence band spectra of the sample SnO_2:$Li_{0.3}$ acquired under conditions of "off resonance" (E_v=50 eV) and "on-resonance" (E_v=59 eV). c) Valence band spectra of the sample SnO_2:$Ni_{0.3}$

acquired under conditions of "out of resonance" (E_v=848 eV) and "on-resonance" (E_v=852.9 eV) according to the Ni $L_{3,2}$ edge XAS spectrum in Figure S2.

The valence band region is composed of three main contributions centered at around 5 eV, 8 eV and 10.5 eV, as shown in Figure 6. The low energy bands at 5 and 8 eV correspond to the O(2p) states and hybridization from the O(2p) and Sn(5p) orbitals, respectively, as commonly reported for SnO_2 [45]. The shoulder at ~10.5 eV can be related to the hybridization between the O(2p) and Sn(5s) orbitals [46]. Only for the samples with the highest amount of dopants, a decrease in the position of the Fermi level with respect to the maximum of the valence band was observed, as compared with undoped SnO_2. The E_F-E_{VBM} decreases about 0.2 eV and 1.2 eV for the samples doped with Li (x=0.3) or Ni (x=0.3), respectively. Hence lower n-type character can be induced by Li or Ni doping (x=0.3) due to compensating effects. Substitutional Li is considered to be promoted by increased Li doping, as suggested by XPS measurements, acting as an acceptor and thus leading to lower n-type character of the samples. Similar phenomena have been previously reported for Li doped SnO_2 [19] indicating a subtitutional incorporation of Li atoms in SnO_2. Reduction of Ni^{3+} to Ni^{2+} by capturing a free electron could be associated with the lower n-type character observed for the Ni (x=0.3) doped samples.

XAS measurements in total electron yeild (TEY) have been also performed on the undoped and Ni, Li doped SnO_2 nanostructures (supplementary Figure S2), also showing small variations due to the Li or Ni doping.

In order to better understand the states in the valence band closer to the Fermi level, resonant photoemission spectroscopy (RPES) was employed. RPES can provide element-specific information on electronic states in valence band. The electronic states can be enhanced when the incident photon energy is slightly higher than the binding energy of the selected core level [47,48]. On-resonance RPES spectra for Ni and Li states were acquired using energies of 853 eV and 59 eV for the samples SnO_2:$Ni_{0.3}$ and SnO_2:$Li_{0.3}$, respectively (based on XAS measurements shown in Figure S2). For the "off resonance" XPS spectra energies of 848 eV and 50 eV, respectively, were used. Figure 6b indicates that there are no clear Li-related states which resonate in the corresponding valence band region, as both "on-resonance" and "off-resonance" spectra are similar. On the other hand, differences can

be appreciated in the region closer to the Fermi level from the SnO_2:$Ni_{0.3}$ sample (Figure 6c) due to Ni-related states which resonate, thus showing higher relative intensity due to the enhanced absorption at 852.9 eV, as enlarged in the inset in Figure 6c. The O(2p)-Ni(3d) hybridization should be related to the increase in the relative intensity of the contribution around 8 eV [49]

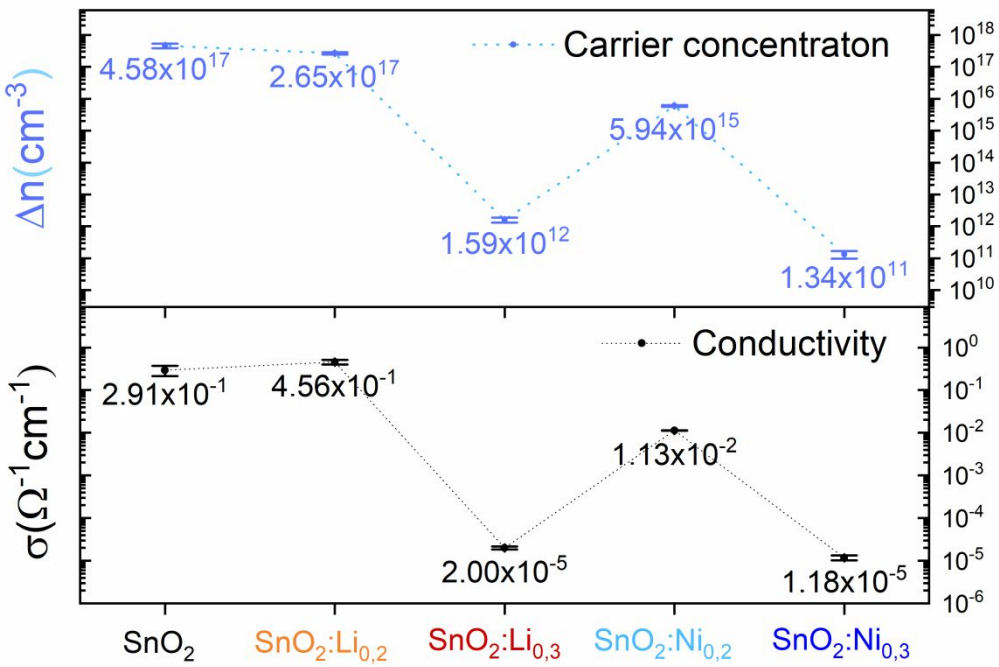

Figure 7. Variation in the charge carrier concentration and the conductivity of the undoped and doped SnO_2 nanoparticles as a function of the doping.

Finally, Hall effect measurements were performed at room temperature on the samples in order to investigate their electrical properties. Prior to the electrical study, the nanoparticles were pressed into pellets. The calculated values corresponding to the conductivity and charge carrier concentration are shown in Figure 7, which is depicted in a logarithmic scale. All Hall effect coefficients obtained were always negative, indicating a clear n-type behaviour. The incorporation of Li and Ni dopants in the amounts considered in this work does not give rise to p conductivity, although some compensation effect on the conductivity is observed for the nanoparticles with the highest concentration of Li and for both Ni doped samples, showing a reduced conductivity when compared with the undoped one. This

compensating effect is in agreement with the reduced n type character detected by XPS Valence Band measurements for Li(x=0.3) and Ni(x=0.3) doped samples. The behaviour of the sample with the lowest Li incorporation could be due to the incorporation of Li as an interstitial following also the trends observed in the XPS Li (1s) results, which indicate that Li could be incorporated as an interstitial for low contents, whereas for higher contents substitutional positions could be preferred. Theorical DFT calculations [50] also support that Li acts as a donor when incorporated as a interstitial, which could explain the small increase in the conductivity for sample Li (x=0.2), whereas it acts as an acceptor when incorporated as a substitutional atom in the SnO_2 lattice compensating the carriers in the SnO_2 and reducing the conductivity for Li (X=0.3) sample. SnO_2 exhibits n-type conductivity due to the formation of oxygen vacancies and Sn interstitial defects, which energy levels are close to the conduction band [51]. Conductivity mechanism on SnO_2 is often studied as thin films. As nanoparticle materials, conductivities are in the order of 10^{-1}-10^{-2} $\Omega^{-1}cm^{-1}$,[52] while doping with elements such as Sb can lead to an increase of the n-type behaviour and conductivity[53] due to the introduction of donor centres near CB . Increase of conductivity is often related to oxygen vacancies. However at the nanoscale, some aspects related to the interface-related processes, hopping mechanisms or percolation effects should be also considered [54]

In this case undoped SnO_2 sample shows averaged conductivity of 2.91 10^{-1} $\Omega^{-1}cm^{-1}$ and carrier concentration of 4.58 10^{17} cm^{-3}, which is in accordance with typical values around 10^{17} -10^{20} cm^{-3} reported for SnO_2 nanoparticles Low Li or Ni doping either improves or decreases, respectively, the corresponding electrical conductivity values. In particular, the sample SnO_2:$Li_{0.2}$ shows a slight increase of the conductivity value, as shown in Figure 7. On the other hand, by increasing the dopant concentration, a lowering of the conductivity is caused both for Li and Ni doping. In that case, values around 10^{-5} $\Omega^{-1}cm^{-1}$ were obtained for SnO_2:$Li_{0.3}$ and SnO_2:$Ni_{0.3}$.

After the initial structural, morphological, electrical, and compositional characterization of the undoped and doped (Li, Ni) SnO_2 nanoparticles, which confirms the high crystalline quality of the as-synthesized nanomaterial and the variable structure of defects associated with the doping process, their implementation in LiB anodes was evaluated.

Figure 8 shows the specific capacity upon cycling from the LiB with anodes based on the synthesized nanomaterial. For all the samples, high initial capacity values were achieved, followed by stable capacity profiles around 500 mAh/g. These apparently high capacity values could be understood due to the small size of the employed nanoparticles [55], as confirmed by XRD and TEM, and the highly conductivity and mobility of the blend. The nanoparticles used in this work offer short distances for charge carriers diffusion and are able to better withstand the volume change, hence improving the capability, although nanoparticles aggregation after several cycles can also lower the cyclability. Actually, J. Chen [56] reported that 10 nm is the critical size to prevent pulverization and aggregation of nanoparticles which degenerate the electrochemical performance in LiB based on previous works.

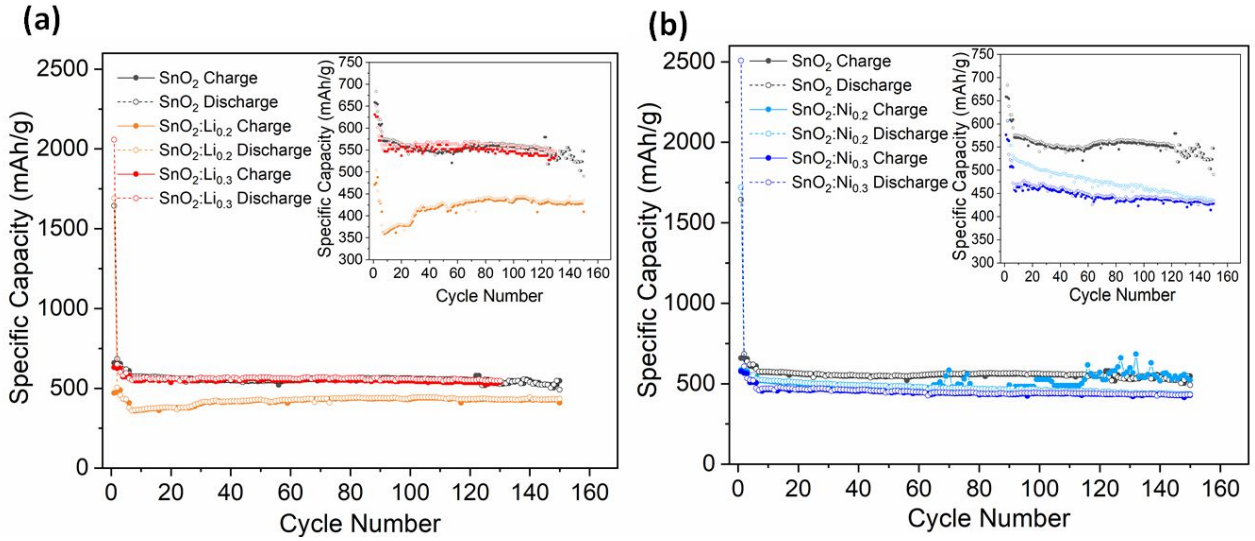

Fig. 8: Specific capacity values upon cycling from LiB with anodes based in (a) Li doped or (b) Ni doped SnO_2 nanoparticles. Values from undoped SnO_2 nanoparticles-based anodes are also included as a reference.

According to the results shown in Figure 8, SnO_2 based cells exhibit an initial specific capacity of 1644 mAh/g, while SnO_2:$Li_{0.2}$, SnO_2:$Li_{0.3}$, SnO_2:$Ni_{0.2}$ and SnO_2:$Ni_{0.3}$ based cells show initial specific capacity values of 1690, 2057, 1718 and 2507 mAh/g, respectively. Unusual high initial capacity values were obtained in this work for the samples with the highest dopant concentration, mainly for SnO_2:$Ni_{0.3}$. Similar results of

Nickel-doped SnO_2 based anodes [57] have been measured with other binders, showing high initial specific capacity but a decrease over time.

The standard behaviour of the anodes based on SnO_2 consist of a high initial capacity which is drastically reduced after the first cycle due to an irreversible conversion reaction of SnO_2 with Li [58]. Besides, the capacity commonly shows a further brisk reduction over the first 30 to 50 cycles, usually attributed, in a generic way, to SnO_2 structural instabilities due to volume expansion/reduction and reactions which occur during lithiation/delithiation processes causing a fading capacity and ultimate disintegration of the anode material. The irreversible conversion reaction causes the initial drop in capacity [59], whereas the main alloy reactions, mostly reversible, lead after few cycles to less Sn^0 reversely converted to SnO_x and the incomplete SnO_2 reduction occurred during lithiation and delithiation, which causes a steady decrease in specific capacity [58]. Moreover, some authors [55] recently reported that conversion and alloying reactions can overlap upon cycling and intermediate Li-Sn-O compounds can be also formed, which should be considered as well in the comprehension of the LiB's electrochemical stability. Other authors point out that the capacity fading was due to interfacial charging of lithium at the phase boundaries of nanoparticles in the SnO_2 electrode [60]. In addition, the decrease of capacity can be also understood with the possible formation of a Solid Electrolyte Interphase (SEI) [60]. In our case, promising 500 – 600 mAh/g capacity values are retained after 150 cycles, hence the presence of dopants and related defects, together with the lack of Sn^{2+} confirmed by XPS in the nanomaterial, could retard some of these intermediate reactions leading to improved cyclability and electrochemical response. It should be remarked that in the present work the capacity fading upon cycling is weaker as compared with some other works [61], which can be partially explained based on the homogeneity, the high crystallinity, and low size of the particles, shortening the diffusion path of lithium and enhancing charge/discharge processes.

In this case, after the first discharge, stable capacity profiles are obtained for all the cells and reversible capacity values between 500 – 600 mAh/g are retained upon 150 cycles or more (Figure 8), which is significantly higher than the theoretical capacity of a graphite anode commercialized (~372 mAh/g) [62], thus confirming excellent cyclability performance.

The stability of these batteries are comparable with previous reports [63] obtained using carbon black and carbon nanotubes. Actually, similar capacity values have been reported for GO/SnO_2 batteries [64], although in that case the good conductivity and mechanical properties of graphene oxide played a key role. Besides, in the present work, Coulombic efficiency values near 100 % were obtained, as shown in Supplementary Figure S3, which confirms the good electrochemical performance of the SnO_2-based cells.

Table 3: Specific capacity at 100 cycles

Sample	**Step**	**C_{esp}(mAh/g)**
SnO_2	Charge	557.1
	Discharge	562.9
SnO_2:$Li_{0.2}$	Charge	431.2
	Discharge	438.3
SnO_2:$Li_{0.3}$	Charge	547.0
	Discharge	560.5
SnO_2:$Ni_{0.2}$	Charge	526.1
	Discharge	458.6
SnO_2:$Ni_{0.3}$	Charge	439.7
	Discharge	442.8

Capacity values after 100 cycles corresponding to the cells with anodes based on undoped or doped SnO_2 nanoparticles are indicated in Table 3, in order to compare the capacity retention for all the cells. After 100 cycles, the reference SnO_2 sample shows 562.9 mAh/g specific capacity and a very stable profile. SnO_2:$Li_{0.2}$ based anodes exhibit a large initial decrease in the capacity followed by a recovery during the followed cycles, although better performance is achieved for SnO_2:$Li_{0.3}$ anodes, with increased oxygen deficiency, as cofirmed by PL. Regarding the lower conductivity of the SnO_2:$Li_{0.3,}$ the anodes based on these nanomaterial exhibit improved capacity and cyclability, as compared with SnO_2:$Li_{0.2}$ based anodes (Figure 8). Hence, enhanced conductivity by doping does not always lead to

better electrochemical performance. This effect can be understood based on the variable Li incorporation as substitutional and interstitial sites as a function of the Li concentration in the SnO_2 lattice. In addition, the enhanced oxygen deficiency described for the SnO_2:$Li_{0.3}$ and the variable structure of defects associated with the doping process, as well as the possible presence of pores or channels in the nanoparticles, could lead to improved lithiation and delithiation processes.

While Li doped SnO_2-based anodes show improved capacity for higher Li doping (SnO_2:$Li_{0.3}$), for Ni doping the opposite behaviour was observed. Low Ni doping involves slighlty higher capacity as compared with SnO_2:$Ni_{0.3}$ samples, although slightly better stability is achieved for the latter. PL and Raman measurements confirmed a high concentration of defects for these nanoparticles, which could hinder the electrochemical performance of the SnO_2:$Ni_{0.3}$ based anodes.

Variable incorporation of dopants in SnO_2, even in a very low concentration, clearly modifies the battery performance, as observed in this work. According to our results, interstitial Li could be favoured at the low doping values, SnO_2:$Li_{0.2}$, while higher doping levels lead also to substitutional Li. Wang et al. [65] analyzed Li doped SnO_2 thin films and proposed the presence of Li interstitials at low Li doping, due to their lowest formation energy, as well as enhanced Li incorporation in Sn sites at higher Li doping. Rahman et al. [50] studied by first principle calculations the incorporation of Li in the rutile SnO_2 lattice and the relation with native defects from the oxide. According to their reported calculations, energy formation of Li interstitials is the lowest, although incorporation of Li at Sn sites is also favourable as lowers the lattice distortion. Li incorporation also reduces the formation energy of native defects in SnO_2 and favours their stabilization. Variable incorporation of dopants as interstitial and/or substitutional has been also reported by other authors, which should be also considered for the Ni doped SnO_2 nanoparticles analyzed in this work. In this case, higher Ni doping induces more defective nanoparticles with decreased conductivity.

The presence of a low amount of Li, preferentially as interstitial, could worsen the lithiation/delithiation processes leading to lower battery performance, as compared with undoped SnO_2, while these processes would be recovered in SnO_2:$Li_{0.3}$ based anodes, for

which the presence of Li in Sn sites, involving higher oxygen vacancies concentration and lower n-type character due to Li-related acceptor levels have been proposed. Ni doping involves combined oxidation states and higher formation of defects leading to lower n-type character and worse conductivity values as compared with undoped SnO_2, although good cyclability is achieved in the Ni doped SnO_2 based LiB anodes.

4. Conclusions

Large amounts of high-crystalline undoped and Li or Ni doped SnO_2 nanoparticles with homogeneous dimensions around 10 nm and tailored composition have been achieved by hydrolisis synthesis. These nanoparticles were used as anodes in LiB showing high capacity values and significant cyclability over 150 cycles. In particular, SnO_2 and SnO_2:$Li_{0.3}$ based anodes exhibit promising capacity values over 560 mAh/g after 100 cycles. In this work fundamental knowledge has been gained based on the study of these nanoparticles by different complementary techniques, hence leading to valuable support to improve the design of new generation LiB. Raman spectra show significant variations in the SnO_2 vibrational modes, despite the low doping concentration in some of the probed samples. High Ni doping induces an increase in the concentration of defects, while variable Li incorporation induces changes mainly in the A_{1g} and E_g modes which can involve variable dopant incorporation in the SnO_2 lattice. PL spectra from the nanoparticles consist in a wide emission centered around 2-2.5 eV. In this case, an increase in the oxygen vacancies concentration can be induced in the SnO_2 nanoparticles with higher Li content, while high Ni doping involves a luminescence quenching due to the formation of large amount of non-radiative recombination centers. XPS measurements confirm the only presence of Sn^{4+} in the Sn 3d core levels for all the samples. Contrary to other previous works, bands related to reduced oxidation states (Sn^{2+}) were not observed in this case. Changes in the Li 1s signal could be related to the coexistence of interstitial and substitutional Li, being the latter promoted in the SnO_2:$Li_{0.3}$ samples. Mixed Ni^{2+}/Ni^{3+} states can be estimated from the analysis of the Ni 3p core levels. The analysis of the valence band regions shows lower n-type character for the samples with higher doping content, mainly for the SnO_2:$Ni_{0.3}$. Finally, Hall effect measurements were performed, and only for low lithium doping an

increase in the conductivity was observed, whereas for the rest of dopings a decrease conductivity and carrier density were measured.

Based on these results, the defect structure associated with the Li or Ni doping, variable Li incorporation as interstitial and substitutional, mixed Ni oxidation states, and the lack of Sn^{2+} confirmed by XPS, could retard some of the intermediate reactions occurred in the LiB, which can be related to the improved cyclability and electrochemical response observed in this case. These aspects should be considered in order to design LiB batteries with enhanced performance.

Supporting information

PL spectra with gaussian deconvolutions of SnO_2 nanoparticles. Sn $M_{4,5}$, O K edge and XAS spectra of doped and undoped SnO_2 nanoparticles and Ni $L_{3,2}$ spectra of SnO_2:$Ni_{0.3}$ nanoparticles. Coulombic efficiency of doped and undoped nanoparticles.

Acknowledgements

We acknowledge Elettra Sincrotrone Trieste for providing access to its synchrotron radiation facilities

The work was supported by MINECO/FEDER/M-ERA.Net Cofund projects: RTI2018-097195-B-I00 and PCIN-2017-106. I.P. and S.N. gratefully acknowledge financial support from EUROFEL

References

(1) Lee, S. Y.; Park, K. Y.; Kim, W. S.; Yoon, S.; Hong, S. H.; Kang, K.; Kim, M. Unveiling Origin of Additional Capacity of SnO2 Anode in Lithium-Ion Batteries by Realistic Ex Situ TEM Analysis. *Nano Energy* **2016**, *19*, 234–245. https://doi.org/10.1016/j.nanoen.2015.10.026.

(2) Poizot, P.; Laruelle, S.; Grugeon, S.; Dupont, L.; Tarascon, J. M. Nano-Sized Transition-Metal Oxides as Negative-Electrode Materials for Lithium-Ion Batteries. *Nature* **2000**, *407* (6803), 496–499. https://doi.org/10.1038/35035045.

(3) Zhang, L.; Wu, H. Bin; Liu, B.; Lou, X. W. Formation of Porous SnO2 Microboxes via Selective Leaching for Highly Reversible Lithium Storage. *Energy Environ. Sci.* **2014**, *7* (3), 1013–1017. https://doi.org/10.1039/c3ee43305f.

(4) Priyadharshini, E.; Suresh, S.; Gunasekaran, S.; Srinivasan, S.; Manikandan, A. Investigation on Electrochemical Performance of SnO2-Carbon Nanocomposite as Better Anode Material for Lithium Ion Battery. *Phys. B Condens. Matter* **2019**, *569*, 8–13. https://doi.org/10.1016/j.physb.2019.05.029.

(5) Yoo, H.; Lee, G.; Choi, J. Binder-Free SnO2-TiO2 Composite Anode with High Durability for Lithium-Ion Batteries. *RSC Adv.* **2019**, *9* (12), 6589–6595. https://doi.org/10.1039/c8ra10358e.

(6) Liu, R.; Su, W.; Shen, C.; Iocozzia, J.; Zhao, S.; Yuan, K.; Zhang, N.; Wang, C. an; Lin, Z. Hydrothermal Synthesis of Hollow SnO2 Spheres with Excellent Electrochemical Performance for Anodes in Lithium Ion Batteries. *Mater. Res. Bull.* **2017**, *96*, 443–448. https://doi.org/10.1016/j.materresbull.2017.03.004.

(7) Agubra, V. A.; Zuniga, L.; Flores, D.; Campos, H.; Villarreal, J.; Alcoutlabi, M. A Comparative Study on the Performance of Binary SnO2/NiO/C and Sn/C Composite Nanofibers as Alternative Anode Materials for Lithium Ion Batteries. *Electrochim. Acta* **2017**, *224*, 608–621. https://doi.org/10.1016/j.electacta.2016.12.054.

(8) Li, F.; Tang, D. M.; Jian, Z.; Liu, D.; Golberg, D.; Yamada, A.; Zhou, H. Li-O2 Battery Based on Highly Efficient Sb-Doped Tin Oxide Supported Ru Nanoparticles. *Adv. Mater.* **2014**, *26* (27), 4659–4664. https://doi.org/10.1002/adma.201400162.

(9) Mueller, F.; Bresser, D.; Chakravadhanula, V. S. K.; Passerini, S. Fe-Doped SnO2 Nanoparticles as New High Capacity Anode Material for Secondary Lithium-Ion Batteries. *J. Power Sources* **2015**, *299*, 398–402. https://doi.org/10.1016/j.jpowsour.2015.08.018.

(10) Prado, F. del; Andersen, H. F.; Taeño, M.; Mæhlen, J. P.; Ramírez-Castellanos, J.; Maestre, D.; Karazhanov, S.; Cremades, A. Comparative Study of the Implementation of Tin and Titanium Oxide Nanoparticles as Electrodes Materials in Li-Ion Batteries. *Sci. Rep.* **2020**, *10* (1), 1–8. https://doi.org/10.1038/s41598-020-62505-x.

(11) Chiu, H. C.; Yeh, C. S. Hydrothermal Synthesis of SnO2 Nanoparticles and Their Gas-Sensing of Alcohol. *J. Phys. Chem. C* **2007**, *111* (20), 7256–7259. https://doi.org/10.1021/jp0688355.

(12) Aziz, M.; Saber Abbas, S.; Wan Baharom, W. R. Size-Controlled Synthesis of SnO2 Nanoparticles by Sol-Gel Method. *Mater. Lett.* **2013**, *91*, 31–34. https://doi.org/10.1016/j.matlet.2012.09.079.

(13) Liu, Y.; Koep, E.; Liu, M. A Highly Sensitive and Fast-Responding SnO2 Sensor Fabricated by Combustion Chemical Vapor Deposition. *Chem. Mater.* **2005**, *17* (15), 3997–4000. https://doi.org/10.1021/cm050451o.

(14) Letsholathebe, D.; Magdalane, C. M.; Poovaragan, S.; Thema, F. T.; Kaviyarasu, K.; Mola, G. T.; Sundaram, R.; Kanimozhi, K.; Anbarasu, M.; Arularasu, M. V; Maaza, M. Structural, Optical, Morphological and Microbial Studies on SnO2 Nanoparticles Prepared by Co-Precipitation Method. *J. Nanosci. Nanotechnol.* **2017**, *18* (5), 3511–3517. https://doi.org/10.1166/jnn.2018.14658.

(15) Del Prado, F.; Cremades, A.; Maestre, D.; Ramírez-Castellanos, J.; González-Calbet, J. M.; Piqueras, J. Controlled Synthesis of Lithium Doped Tin Dioxide Nanoparticles by a Polymeric

Precursor Method and Analysis of the Resulting Defect Structure. *J. Mater. Chem. A* **2018**, *6* (15), 6299–6308. https://doi.org/10.1039/c7ta09324a.

(16) García-Tecedor, M.; Maestre, D.; Cremades, A.; Piqueras, J. Influence of Cr Doping on the Morphology and Luminescence of SnO2 Nanostructures. *J. Phys. Chem. C* **2016**, *120* (38), 22028–22034. https://doi.org/10.1021/acs.jpcc.6b06682.

(17) García-Tecedor, M.; del Prado, F.; Bueno, C.; Cristian Vásquez, G.; Bartolomé, J.; Maestre, D.; Díaz, T.; Cremades, A.; Piqueras, J. Tubular Micro- and Nanostructures of TCO Materials Grown by a Vapor-Solid Method. *AIMS Mater. Sci.* **2016**, *3* (2), 434–447. https://doi.org/10.3934/matersci.2016.2.434.

(18) García-Tecedor, M.; Maestre, D.; Cremades, A.; Piqueras, J. Growth and Characterization of Cr Doped SnO_2 Microtubes with Resonant Cavity Modes. *J. Mater. Chem. C* **2016**, *4* (24), 5709–5716. https://doi.org/10.1039/C6TC01632D.

(19) Prado, F. del; Cremades, A.; Maestre, D.; Ramírez-Castellanos, J.; González-Calbet, J. M.; Piqueras, J. Controlled Synthesis of Lithium Doped Tin Dioxide Nanoparticles by a Polymeric Precursor Method and Analysis of the Resulting Defect Structure. *J. Mater. Chem. A* **2018**, *6* (15), 6299–6308. https://doi.org/10.1039/C7TA09324A.

(20) Peche-Herrero, M. A.; Maestre, D.; Ramírez-Castellanos, J.; Cremades, A.; Piqueras, J.; González-Calbet, J. M. The Controlled Transition-Metal Doping of SnO2 Nanoparticles with Tunable Luminescence. *CrystEngComm* **2014**, *16* (14), 2969. https://doi.org/10.1039/c3ce42188k.

(21) Mueller, F.; Bresser, D.; Chakravadhanula, V. S. K.; Passerini, S. Fe-Doped SnO2 Nanoparticles as New High Capacity Anode Material for Secondary Lithium-Ion Batteries. *J. Power Sources* **2015**, *299*, 398–402. https://doi.org/10.1016/j.jpowsour.2015.08.018.

(22) Ma, Y.; Ma, Y.; Ulissi, U.; Ji, Y.; Streb, C.; Bresser, D.; Passerini, S. Influence of the Doping Ratio and the Carbon Coating Content on the Electrochemical Performance of Co-Doped SnO2 for Lithium-Ion Anodes. *Electrochim. Acta* **2018**, *277*, 100–109. https://doi.org/10.1016/j.electacta.2018.04.209.

(23) Zangrando, M.; Finazzi, M.; Paolucci, G.; Comelli, G.; Diviacco, B.; Walker, R. P.; Cocco, D.; Parmigiani, F. BACH, the Beamline for Advanced Dichroic and Scattering Experiments at ELETTRA. *Rev. Sci. Instrum.* **2001**, *72* (2), 1313–1319. https://doi.org/10.1063/1.1334626.

(24) Zangrando, M.; Zacchigria, M.; Finazzi, M.; Cocco, D.; Rochow, R.; Parmigiani, F. Polarized High-Brilliance and High-Resolution Soft x-Ray Source at ELETTRA: The Performance of Beamline BACH. *Rev. Sci. Instrum.* **2004**, *75* (1), 31–36. https://doi.org/10.1063/1.1634355.

(25) Amutha, T.; Rameshbabu, M.; Sasi Florence, S.; Senthilkumar, N.; Vetha Potheher, I.; Prabha, K. Studies on Structural and Optical Properties of Pure and Transition Metals (Ni, Fe and Co-Doped Ni–Fe) Doped Tin Oxide (SnO2) Nanoparticles for Anti-Microbial Activity. *Res. Chem. Intermed.* **2019**, *45* (4), 1929–1941. https://doi.org/10.1007/s11164-018-03713-z.

(26) Shannon, R. D. Revised Effective Ionic Radii in Halides and Chalcogenides. *Acta Crystallogr.* **1976**, No. A32, 751. https://doi.org/10.1107/S0567739476001551.

(27) Tabassum, S.; Shafeeq M., M.; Naqvi, A. H.; Azam, A.; Singla, M. L.; Ahmed, A. S. Band Gap

Narrowing and Fluorescence Properties of Nickel Doped SnO2 Nanoparticles. *J. Lumin.* **2010**, *131* (1), 1–6. https://doi.org/10.1016/j.jlumin.2010.07.017.

(28) Ben Haj Othmen, W.; Sieber, B.; Elhouichet, H.; Addad, A.; Gelloz, B.; Moreau, M.; Szunerits, S.; Boukherroub, R. Effect of High Fe Doping on Raman Modes and Optical Properties of Hydrothermally Prepared SnO2 Nanoparticles. *Mater. Sci. Semicond. Process.* **2018**, *77*, 31–39. https://doi.org/10.1016/j.mssp.2017.12.014.

(29) Diéguez, A.; Romano-Rodŕiguez, A.; Vilà, A.; Morante, J. R. The Complete Raman Spectrum of Nanometric SnO2 Particles. *J. Appl. Phys.* **2001**, *90* (3), 1550–1557. https://doi.org/10.1063/1.1385573.

(30) Peche-Herrero, M. A.; Maestre, D.; Ramírez-Castellanos, J.; Cremades, A.; Piqueras, J.; González-Calbet, J. M. The Controlled Transition-Metal Doping of SnO2 Nanoparticles with Tunable Luminescence. *CrystEngComm* **2014**, *16* (14), 2969–2976. https://doi.org/10.1039/c3ce42188k.

(31) Bhatnagar, M.; Kaushik, V.; Kaushal, A.; Singh, M.; Mehta, B. R. Structural and Photoluminescence Properties of Tin Oxide and Tin Oxide: C Core-Shell and Alloy Nanoparticles Synthesised Using Gas Phase Technique. *AIP Adv.* **2016**, *6*, 95321. https://doi.org/10.1063/1.4964313.

(32) Kar, A.; Kundu, S.; Patra, A. Surface Defect-Related Luminescence Properties of SnO2 Nanorods and Nanoparticles. *J. Phys. Chem. C* **2011**, *115* (1), 118–124. https://doi.org/10.1021/jp110313b.

(33) Tabei, M.; Shionoya, S.; Ohmatsu, H. Mechanism of the Killer Effect of Iron-Group Ions on the Green Luminescence in ZnS:Cu, Al Phosphors. *Jpn. J. Appl. Phys.* **1975**, *14* (2), 240–247. https://doi.org/10.1143/JJAP.14.240.

(34) Zhou, G.; Ni, S.; Sun, X.; Wang, X.; Wang, Q.; He, D. Visible Photoluminescence of Hydrothermal Synthesized Sn1-x Ni x O2 Nanostructures. *J. Mater. Sci. Mater. Electron.* **2011**, *22* (2), 174–178. https://doi.org/10.1007/s10854-010-0109-8.

(35) Korusenko, P. M.; Nesov, S. N.; Bolotov, V. V.; Povoroznyuk, S. N.; Pushkarev, A. I.; Ivlev, K. E.; Smirnov, D. A. Formation of Tin-Tin Oxide Core-Shell Nanoparticles in the Composite SnO2-x Nitrogen-Doped Carbon Nanotubes by Pulsed Ion Beam Irradiation. *Nucl. Instruments Methods Phys. Res. Sect. B Beam Interact. with Mater. Atoms* **2017**, *394* (March), 37–43. https://doi.org/10.1016/j.nimb.2016.12.037.

(36) NIST Standard Reference Database. NIST X-Ray Photoelectron Spectroscopy Database. *Natl. Inst. Stand. Technol.* **2000**, *20*. https://doi.org/10.18434/T4T88.

(37) Willemen, H.; Van De Vondel, D. F.; Van Der Kelen, G. P. An ESCA Study of Tin Compounds. *Inorganica Chim. Acta* **1979**, *34* (C), 175–180. https://doi.org/10.1016/S0020-1693(00)94698-X.

(38) Stranick, M. A.; Moskwa, A. SnO_2 by XPS. *Surf. Sci. Spectra* **1993**, *2* (1), 50–54. https://doi.org/10.1116/1.1247724.

(39) Qiao, L.; Bi, X. Direct Observation of Ni3+ and Ni2+ in Correlated LaNiO3-δ Films. *Epl* **2011**, *93* (5), 57002. https://doi.org/10.1209/0295-5075/93/57002.

(40) Wang, M.; Zhao, T.; Li, M.; Wang, H. Perovskite La 2 (NiCu)O 4 Catalyst Precursors for Dry Reforming of Methane: Effects of Cu-Substitution on Carbon Resistance. *RSC Adv.* **2017**, *7* (66), 41847–41854. https://doi.org/10.1039/c7ra08422f.

(41) Meeporn, K.; Chanlek, N.; Thongbai, P. Effects of DC Bias on Non-Ohmic Sample-Electrode Contact and Grain Boundary Responses in Giant-Permittivity La1.7Sr0.3Ni1-XMgxO4 Ceramics. *RSC Adv.* **2016**, *6* (94), 91377–91385. https://doi.org/10.1039/c6ra19290d.

(42) San Choi, J.; Ahn, C. W.; Bae, J. S.; Kim, T. H. Identifying a Perovskite Phase in Rare-Earth Nickelates Using X-Ray Photoelectron Spectroscopy. *Curr. Appl. Phys.* **2020**, *20* (1), 102–105. https://doi.org/10.1016/j.cap.2019.10.013.

(43) Ullah Awan, S.; Hasanain, S. K.; Bertino, M. F.; Hassnain Jaffari, G. Ferromagnetism in Li Doped ZnO Nanoparticles: The Role of Interstitial Li. *J. Appl. Phys.* **2012**, *112* (10). https://doi.org/10.1063/1.4767364.

(44) Kumar, P.; Yadav, A. K.; Bhattacharyya, D.; Jha, S. N.; Pandey, P. C. Lithium Ion Assisted Luminescence and Ferromagnetism in Europium Doped Zinc Oxide. *Mater. Chem. Phys.* **2018**, *214*, 306–319. https://doi.org/10.1016/j.matchemphys.2018.04.080.

(45) Themlin, J. M.; Sporken, R.; Darville, J.; Caudano, R.; Gilles, J. M.; Johnson, R. L. Resonant-Photoemission Study of SnO2: Cationic Origin of the Defect Band-Gap States. *Phys. Rev. B* **1990**, *42* (18), 11914–11925. https://doi.org/10.1103/PhysRevB.42.11914.

(46) del Prado, F.; Cremades, A.; Ramírez-Castellanos, J.; Maestre, D.; González-Calbet, J. M.; Piqueras, J. Effect of Lithium Doping and Precursors on the Microstructural, Surface Electronic and Luminescence Properties of Single Crystalline Microtubular Tin Oxide Structures. *CrystEngComm* **2017**, *19* (30), 4321–4329. https://doi.org/10.1039/C7CE00856B.

(47) Kay, A.; Arenholz, E.; Mun, S.; García De Abajo, F. J.; Fadley, C. S.; Denecke, R.; Hussain, Z.; Van Hove, M. A. Multi-Atom Resonant Photoemission: A Method for Determining near-Neighbor Atomic Identities and Bonding. *Science (80-.).* **1998**, *281* (5377), 679–683. https://doi.org/10.1126/science.281.5377.679.

(48) Shkvarin, A. S.; Yarmoshenko, Y. M.; Merentsov, A. I.; Píš, I.; Bondino, F.; Shkvarina, E. G.; Titov, A. N. Guest-Host Chemical Bonding and Possibility of Ordering of Intercalated Metals in Transition-Metal Dichalcogenides. *Inorg. Chem.* **2018**, *57* (9), 5544–5553. https://doi.org/10.1021/acs.inorgchem.8b00511.

(49) Zhang, K. H. L.; Wu, R.; Tang, F.; Li, W.; Oropeza, F. E.; Qiao, L.; Lazarov, V. K.; Du, Y.; Payne, D. J.; Macmanus-Driscoll, J. L.; Blamire, M. G. Electronic Structure and Band Alignment at the NiO and SrTiO3 P-n Heterojunctions. *ACS Appl. Mater. Interfaces* **2017**, *9* (31), 26549–26555. https://doi.org/10.1021/acsami.7b06025.

(50) Rahman, G.; Din, N. U.; García-Suárez, V. M.; Kan, E. Stabilizing Intrinsic Defects in SnO2. *Phys. Rev. B - Condens. Matter Mater. Phys.* **2013**, *87* (20), 1–10. https://doi.org/10.1103/PhysRevB.87.205205.

(51) Kılıç, Ç.; Zunger, A. Origins of Coexistence of Conductivity and Transparency in SnO2. *Phys. Rev. Lett.* **2002**, *88* (9), 955011–955014. https://doi.org/10.1103/PhysRevLett.88.095501.

(52) Rajeeva, M. P.; Naveen, C. S.; Lamani, A. R.; Bothla, V. P.; Jayanna, H. S. Study on Low

Temperature DC Electrical Conductivity of SnO 2 Nanomaterial Synthesized by Simple Gel Combustion Method. In *AIP Conference Proceedings*; American Institute of Physics Inc., 2015; Vol. 1665, p 050091. https://doi.org/10.1063/1.4917732.

(53) Xiaozhen, L.; Jie, C.; Wenbin, S.; Beiling, Q. Complexation-Coprecipitation Synthesis and Characterization of Erbium and Antimony Doped SnO2 Conductive Nanoparticles. *J. Rare Earths* **2007**, *25* (SUPPL. 1), 72–76. https://doi.org/10.1016/S1002-0721(07)60527-4.

(54) Skoromets, V.; Němec, H.; Kopeček, J.; Kužel, P.; Peters, K.; Fattakhova-Rohlfing, D.; Vetushka, A.; Müller, M.; Ganzerová, K.; Fejfar, A. Conductivity Mechanisms in Sb-Doped SnO2 Nanoparticle Assemblies: DC and Terahertz Regime. *J. Phys. Chem. C* **2015**, *119* (33), 19485–19495. https://doi.org/10.1021/acs.jpcc.5b05091.

(55) Böhme, S.; Philippe, B.; Edström, K.; Nyholm, L. Photoelectron Spectroscopic Evidence for Overlapping Redox Reactions for SnO2 Electrodes in Lithium-Ion Batteries. *J. Phys. Chem. C* **2017**, *121* (9), 4924–4936. https://doi.org/10.1021/acs.jpcc.7b01529.

(56) Chen, J. Recent Progress in Advanced Materials for Lithium Ion Batteries. *Materials (Basel).* **2013**, *6* (1), 156–183. https://doi.org/10.3390/ma6010156.

(57) Wan, N.; Zhao, T.; Sun, S.; Wu, Q.; Bai, Y. Nickel and Nitrogen Co-Doped Tin Dioxide Nano-Composite as a Potential Anode Material for Lithium-Ion Batteries. *Electrochim. Acta* **2014**, *143*, 257–264. https://doi.org/10.1016/j.electacta.2014.08.028.

(58) Ferraresi, G.; Villevieille, C.; Czekaj, I.; Horisberger, M.; Novák, P.; El Kazzi, M. SnO2 Model Electrode Cycled in Li-Ion Battery Reveals the Formation of Li2SnO3 and Li8SnO6 Phases through Conversion Reactions. *ACS Appl. Mater. Interfaces* **2018**, *10* (10), 8712–8720. https://doi.org/10.1021/acsami.7b19481.

(59) Chen, J. S.; Lou, X. W. D. SnO2 -Based Nanomaterials: Synthesis and Application in Lithium-Ion Batteries. *Small* **2013**, *9* (11), 1877–1893. https://doi.org/10.1002/smll.201202601.

(60) Smith, M. R.; Johnson, P. L.; Teeters, D. Interfacial Storage of Lithium in the Nanostructure of SnO2 Nanobaskets for Capacities Exceeding Theoretical Values. *Solid State Ionics* **2012**, *225*, 680–684. https://doi.org/10.1016/j.ssi.2011.11.022.

(61) Narsimulu, D.; Vinoth, S.; Srinadhu, E. S.; Satyanarayana, N. Surfactant-Free Microwave Hydrothermal Synthesis of SnO2 Nanosheets as an Anode Material for Lithium Battery Applications. *Ceram. Int.* **2018**, *44* (1), 201–207. https://doi.org/10.1016/j.ceramint.2017.09.159.

(62) Wan, N.; Lu, X.; Wang, Y.; Zhang, W.; Bai, Y.; Hu, Y. S.; Dai, S. Improved Li Storage Performance in SnO2 Nanocrystals by a Synergetic Doping. *Sci. Rep.* **2016**, *6* (1), 18978. https://doi.org/10.1038/srep18978.

(63) Diao, G. Q.; Li, H.; Ivanenko, I.; Dontsova, T.; Astrelin, I.; Xie, F. Y.; Guo, X. Z. Comparison of SnO2 -Carbon Nanotubes Composite and the SnO 2 -Carbon Black Mixture as an Anode for Li-Ion Batteries. *IOP Conf. Ser. Mater. Sci. Eng.* **2019**, *474* (1), 012022. https://doi.org/10.1088/1757-899X/474/1/012022.

(64) Deng, Y.; Fang, C.; Chen, G. The Developments of SnO2/Graphene Nanocomposites as Anode Materials for High Performance Lithium Ion Batteries: A Review. *Journal of Power Sources*. 2016, pp 81–101. https://doi.org/10.1016/j.jpowsour.2015.11.017.

(65) Wang, J.; Zhou, W.; Wu, P. Band Gap Widening and d 0 Ferromagnetism in Epitaxial Li-Doped SnO 2 Films. *Appl. Surf. Sci.* **2014**, *314*, 188–192. https://doi.org/10.1016/j.apsusc.2014.06.144.

For Table of Contents Only